Draft version March 18, 2024
Typeset using LaTeX **twocolumn** style in AASTeX631

The Bright Rim Prominences according to 2.5D Radiative Transfer

Jack M. Jenkins [1], Christopher M. J. Osborne [2], Ye Qiu [3], Rony Keppens [1] and Chuan Li [3,4,5]

[1] *Centre for mathematical Plasma-Astrophysics, Celestijnenlaan 200B, 3001 Leuven, KU Leuven, Belgium*
[2] *SUPA School of Physics and Astronomy, University of Glasgow, Glasgow G12 8QQ, UK*
[3] *Institute of Science and Technology for Deep Space Exploration, Nanjing University, Suzhou 215163, China*
[4] *School of Astronomy and Space Science, Nanjing University, Nanjing 210023, China*
[5] *Key Laboratory for Modern Astronomy and Astrophysics (Nanjing University), Ministry of Education, Nanjing 210023, China*

ABSTRACT

Solar prominences observed close to the limb commonly include a bright feature that, from the perspective of the observer, runs along the interface between itself and the underlying chromosphere. Despite several idealised models being proposed to explain the underlying physics, a more general approach remains outstanding. In this manuscript we demonstrate as a proof-of-concept the first steps in applying the *Lightweaver* radiative transfer framework's 2.5D extension to a 'toy' model prominence + VAL3C chromosphere, inspired by recent 1.5D experiments that demonstrated a significant radiative chromosphere – prominence interaction. We find the radiative connection to be significant enough to enhance both the electron number density within the chromosphere, as well as its emergent intensity across a range of spectral lines in the vicinity of the filament absorption signature. Inclining the viewing angle from the vertical, we find these enhancements to become increasingly asymmetric and merge with a larger secondary enhancement sourced directly from the prominence underside. In wavelength, the enhancements are then found to be the largest in both magnitude and horizontal extent for the spectral line cores, decreasing into the line wings. Similar behaviour is found within new *Chinese Hα Solar Explorer* (CHASE)/*Hα Imaging Spectrograph* (HIS) observations, opening the door for subsequent statistical confirmations of the theoretical basis we develop here.

Keywords: Solar prominences (1519), Solar filaments (1495), Radiative transfer (1335), Solar chromosphere (1479)

1. INTRODUCTION

Solar prominence bright rims have been observed for decades, and in response numerous models have been constructed that aim to explain their origin (Vial & Engvold 2015, and references therein). For example, Heinzel et al. (1995) argued that the underside of a solar prominence scatters more light towards the observer than its overside, making this lower region appear brighter. Paletou (1997) then challenged this conclusion, suggesting that such a process would be unable to explain the magnitude of intensity increase measured for prominence bright rims. Since then, Panasenco (2010) and others have suggested the enhancement may have a chromospheric origin, being instead related to the viewing angle on underlying fibrillar structures that have different thermodynamic properties. The exploratory study of Kostik & Orlova (1975) also considered the phenomenon to be of chromospheric origin, suggesting that radiation trapping–the bouncing back and forth of radiation between the chromosphere and an overlying prominence–may be responsible. Our historical inability to construct self-consistent models of solar prominences, inclusive of radiation, has hindered attempts to validate any one of these theories.

The recent study of Jenkins et al. (2023) highlighted, however, that the classical 1.5D approximation failed for the elevated atmospheres of solar prominences on account of a significant radiative trapping that existed between it and the underlying chromosphere (see also Paletou et al. 1993). The cause of this trapping was found to be the 1.5D plane-parallel approximation that implicitly assumes the prominence to be infinitely hori-

jack.jenkins@kuleuven.be

zontal in extent. Hence, all upwards directed radiation released from the chromosphere encounters the prominence, regardless of the angle of the quadrature, and a non-negligible flux of radiation is then scattered back towards the chromosphere. The result is that this radiation bounces back and forth pumping the populations of the prominence, but also the underlying chromosphere. This trapping was so significant, that it drove the core of the Hydrogen Hα line into positive contrast against the illuminating chromosphere. This is in direct contradiction to the characteristic appearance of Hα filaments as dark channels snaking across the surface of the Sun (*e.g.*, Parenti 2014).

This experiment provided a clear indication that a radiative connection existed between prominences and their underlying chromospheres, at least in 1.5D. In multi-dimensions, prominences are not infinite in extent but neither are they infinitely thin. Moreover, the length of a prominence can often be an order of magnitude longer than its width. Taken together, it is probable that a non-negligible amount of radiation is in any case scattered back towards the chromosphere. The aim of this manuscript is to therefore explore and quantify this radiative interaction.

We introduce the model geometry and 2.5D radiative transfer considerations in Section 2, the principle results are shown in Section 3, before being summarised and discussed in Section 4.

2. METHODS

2.1. *Model Geometry*

We aim herewith to quantify the radiative interaction existing between the solar chromosphere and an isolated solar prominence suspended within the solar corona. For the chromospheric portion of the model, we adopt a modified VAL3C stratification that extends from 92 km below the photosphere to 11 Mm into the solar corona, encompassing the temperature minimum, chromosphere, and transition region in between (Vernazza et al. 1981). Following the approach adopted by RADYN and discussed in Carlsson et al. (2023), the hydrostatic extrapolation of the underlying radiative equilibrium assumes a vertical rather than short-loop geometry. This then invariantly spans a range of -55 – 55 Mm in the horizontal direction.

For the prominence atmosphere, we recently extracted self-consistent prominence atmospheres from `MPI-AMRVAC` magnetohydrodynamic (MHD) simulations, coupling them to semi-empirical models of the solar chromosphere (Jenkins et al. 2023; Keppens et al. 2023). Here we instead construct a 'toy' prominence stratification outside of hydrostatic equilibrium and em-

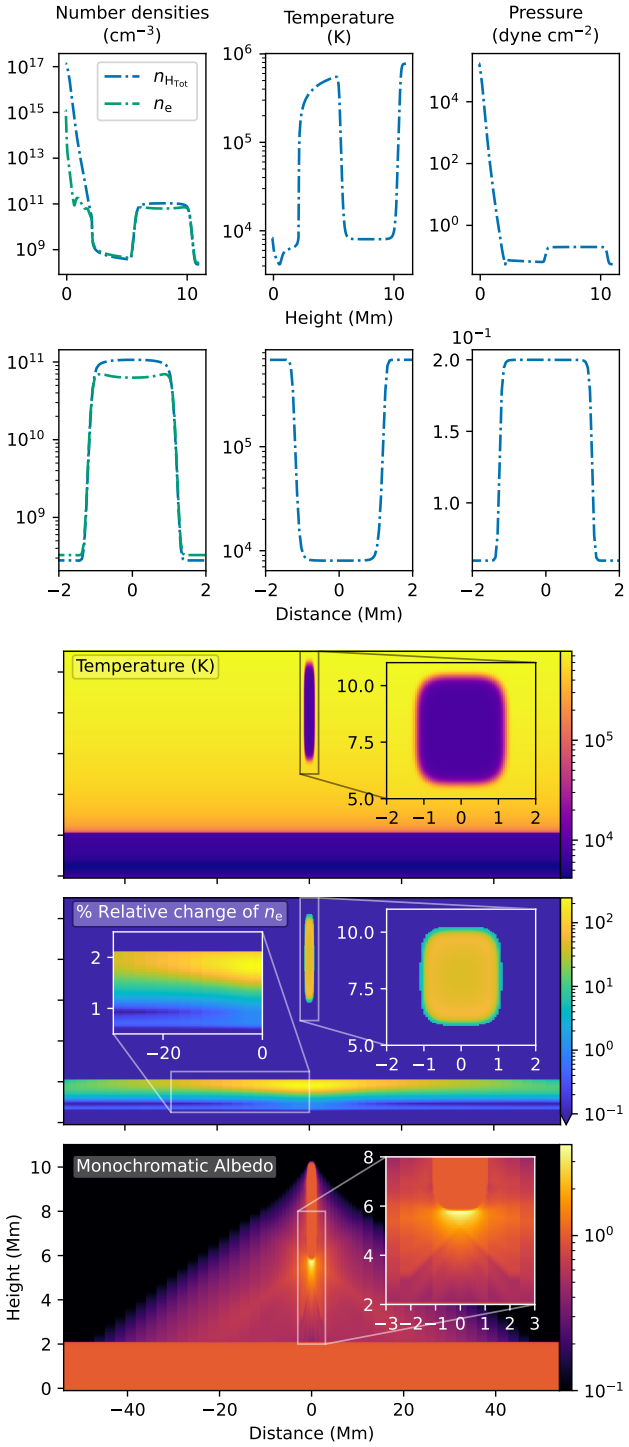

Figure 1. The stratification of the 'toy' prominence model and background atmosphere. The first and second rows present the vertical and horizontal variation, respectively, of the electron and total Hydrogen number densities, temperature, and pressure in the model atmosphere. The bottom three panels present the spatial distribution of temperature, % relative change of n_e (photoionisation), and the angle-integrated monochromatic albedo for the head of the Lyman continuum, respectively, with inset panels zooming in on specific details.

bed it within the modified VAL3C atmosphere (similar to the approach of Díaz Baso et al. 2019). In this way we can concentrate the necessary resolution at the *prominence-corona transition region* (PCTR) interface. We chose the minimum temperature of the prominence core to be a characteristic 8000 K at 0.2 dyn cm^{-2}, with a geometrical extent of 2 Mm and 5 Mm in the horizontal and vertical directions, respectively, centered on (0,8) Mm. We set the shape of the prominence to that of a 'squircle', a unit sphere within the ℓ^p space, to negate numerical oscillations in the interpolation at the sharp corners of a square,

$$|x|^p + |y|^p = r^p, \tag{1}$$

where x and y are the Cartesian coordinates, p is the order of the space, and r the radius of a chosen unit sphere. The specific ℓ^p space of order $p = 4$ and radius $r = 1$ is named the 'squircle', but any radius will benefit from the continuity characteristic. This prominence core is then smoothly connected to the solar corona using the hyperbolic tangent function (cf. Xia et al. 2012),

$$f(x,y) = \frac{\tanh(s \times (r(x,y) - x_{\text{off}})) + y_{\text{off}}}{y_{\text{off}} + 1}, \tag{2}$$

$$T(x,y) = T_{\text{core}} + (f(x,y) \times (T_{\text{VAL3C}}(x,y) - T_{\text{core}})), \tag{3}$$

where $s = 2$ controls the 'steepness' of the tanh() profile, $x_{\text{off}} = 2.5$ Mm, $y_{\text{off}} = 1$ Mm, and $T_{\text{core}} = 8000$ K.

By adopting such a 'toy' model, the gradients in the thermodynamic properties that connect the prominence core with the solar corona, the PCTR, are hydrodynamically idealised and hence differ from the 1D magnetohydrostatic (MHS) class of (K-S type) thread solutions from Heinzel & Anzer (2001) that have been widely adopted (Kippenhahn & Schlüter 1957).

Such solutions do not consider the same temperature ranges as we do and so, in a more hybrid manner, we first ensure the connecting hyperbolic tangent profile closely traces the MHS solutions at the low temperatures of < 20 kK. Above this temperature, the hyperbolic tangent is much sharper than the MHS models and hence closer to those of Gouttebroze (2006), but such temperatures lie outside the range considered applicable for the transitions that we will explore in this manuscript (cf. Carlsson & Leenaarts 2012).

The resulting model domain, alongside 1D cuts of the vertical and horizontal model stratifications, is presented in Figure 1. The model has a vertical resolution of 300 points with a variable δy established following an optimisation routine that distributes and focus these points in locations of strong atmospheric gradients[1]. The horizontal dimension has a resolution of 131, with a δx that focuses the highest resolution around the prominence and varies symmetrically about 0 Mm: ≈ 57 km out to 2 Mm, then 0.8 Mm out to 9 Mm, and finally 2.25 Mm out to the edges of the model.

2.2. *Radiative Transfer*

Throughout this work we will primarily make use of the *Lightweaver* framework. We have previously applied such a framework to the synthesis of a range of solar prominence atmospheres under the 1.5D plane-parallel approximation (Jenkins et al. 2023). Here, we use instead the 2.5D extension recently reported on in Osborne & Fletcher (2022), but without the time-dependent evolution of the rate equations as they employ. Here, the '.5' indicates that all vectors in the 1D and 2D geometries contain two and three components, respectively, that are considered invariant in this extra dimension.

The latest version of *Lightweaver* contains domain decomposition in the vertical direction to facilitate deployment on massively-parallelised machine architectures. This is implemented as sub contexts to the `Context` object in the Python frontend, such that each subdomain acts as fixed boundary conditions to their adjacents. This has the consequence that information has a finite travel distance per iteration, slightly lengthening the time taken to reach convergence. The bottom boundary maintains the diffuse thermalised radiation approximation, and the upper boundary remains 'open' - we consider no incoming radiation from the solar corona.

Lightweaver in 2.5D has two formal solvers implemented, linear or BESSER following the implementation of Štěpán & Trujillo Bueno (2013), of which we employ the latter here. Despite focusing the resolution of the model to the prominence and PCTR, we have adopted linear interpolation as initial tests yielded non-conservation of energy across sharp intensity gradients when using BESSER. This will lead to increased diffusion in the propagation of radiation throughout the model in comparison to a more advanced interpolation method.

Our early tests found that the exact angular quadrature assumed for the discrete propagation of radiation through the domain had direct consequences on the solution. The low order A-2 –A-8 quadrature sets of Carlson (1963) (see also Bruls et al. 1999), the anisotropy-optimised quadratures of Štěpán et al. (2020) and Jaume Bestard et al. (2021), and the Gauss-Legendre(-Trapezoidal in multi-D) sets - commonly employed as

[1] The pTau Python package of J. de la Cruz Rodriguez

ground-truth benchmarks - led to the 'spotlighting' of the prominence-backscattered light on the underlying chromosphere (Paletou 1995). That is, a lack of, asymmetric, or non-uniformly weighted angular resolution, respectively, led to the focusing of the significant backscattered flux into discrete locations at chromospheric heights. Such issues have thusfar gone unreported on account of solar atmospheric models generally not considering the discrete and isolated plasma condensates at elevation that are prominences. To overcome this, we implemented the HEALPix equal weight spherical discretisation of Górski et al. (2005), that has proven useful in other radiative transfer contexts (such as De Ceuster et al. 2020). The utility here lies in the discretisation not introducing any optimisations to the weighting of the individual rays, and so more evenly distributing all of the aforementioned backscattered radiation. The explicit demonstration of these limitations will be presented in full in a subsequent study. We choose the HEALPix set of order 4, containing 100 rays over a half sphere, of which eight contributed halfed weights to the integration to satisfy the symmetry condition.

The bright-rim phenomenon is most commonly reported for prominences close to the limb from the perspective of the observer. At such a position, limb-darkening plays a non-negligible role in the appearance of the background and should be taken into account (Heinzel et al. 1995). At such an extent, limb-darkening is not only angularly dependent but also spatially so; at small μ angles the curvature of the Sun is non-negligible within the field of view (FOV). The model itself assumes a Cartesian geometry, hence the spatial component cannot be taken into account within the model domain. The illumination of the model according to limb darkening is instead included within the boundary conditions (as in Jenkins et al. 2023). Fixing the lateral boundaries in this way ensures the horizontal rays from the HEALPix quadrature, problematic in a periodic model, receive the necessary information. Furthermore, for very small μ angles, the solar limb will be present within the FOV and a self-consistent transition of the model filament to prominence will be possible.

Exactly as for our previous works we consider the same 5 level + continuum hydrogen atom with 10 bound-bound transitions, 5 level + continuum calcium II atom with 5 bound-bound transitions, and 10 level + continuum magnesium II atom with 15 bound-bound transitions. Although we include all of these atoms (hereafter H, Ca II, Mg II) and their transitions in the convergence, we will only focus on the common H and Ca II transitions within this manuscript and reserve the more complex Mg II to a more comprehensive follow-up study. Convergence is considered satisfied when the angle-averaged radiation field J, population levels, and partial frequency redistribution (PRD) ρ reach a maximum relative absolute difference between iterations of 5×10^{-3}, 1.5×10^{-3}, and 1×10^{-4}, respectively.

During the iterations of the population levels, we additionally iterate for the unknown $n_{\rm e}$ using the outside local thermodynamic equilibrium (NLTE) prominence tables of Heinzel et al. (2015) as our initial conditions. This is an important step to take photoionisation by the radiation illuminating the prominence into consideration and, as we shall show later, the influence of its backscattering on the chromosphere. As this iteratively alters the pressure of the equilibrium, we modify $N_{\rm H_{Tot}}$ to maintain the pressure initial conditions and also update the other population levels accordingly (cf. Heinzel et al. 1995; Paletou 1995).

3. RESULTS

3.1. *Converged* $n_{\rm e}$

In 1.5D radiative transfer models of solar prominences, iterating the electron number density during convergence leads to an increase in their population at prominence extremities on account of photoionisation by, for example, the Lyman and Balmer continua (cf. Heinzel et al. 2014; Zapiór et al. 2016). For the 2.5D model here, Figure 1 shows that the iterated electron number density at the edges of the prominence is indeed enhanced relative to the core population, but more modestly than reported in the 1.5D models. Similarly, there appears to be almost no difference in the magnitude of $n_{\rm e}$ within the lower, sun-facing PCTR versus the space-facing side, with the former being a mere 1% larger. Of particular interest is the $n_{\rm e}$ enhancement in the upper layers of the underlying chromosphere that decreases in magnitude with increasing horizontal distance from the prominence. In much the same way, the extent of the enhancement in depth is greatest directly underneath the prominence and decreases with horizontal distance.

In the same Figure, we show the monocromatic albedo (A_ν) at the head (912 Å) of the photoionising Lyman continuum (LyC) following,

$$A_\nu = \frac{\int I^{\rm down}_{LyC}\, d\mu}{\int I^{\rm up}_{LyC}\, d\mu}, \tag{4}$$

wherein the underside of the prominence is shown to scatter a significant amount of incident radiation back towards the solar chromosphere. It is the back and forth of this ionising radiation that leads to the increased $n_{\rm e}$ in both the prominence and its underlying chromosphere.

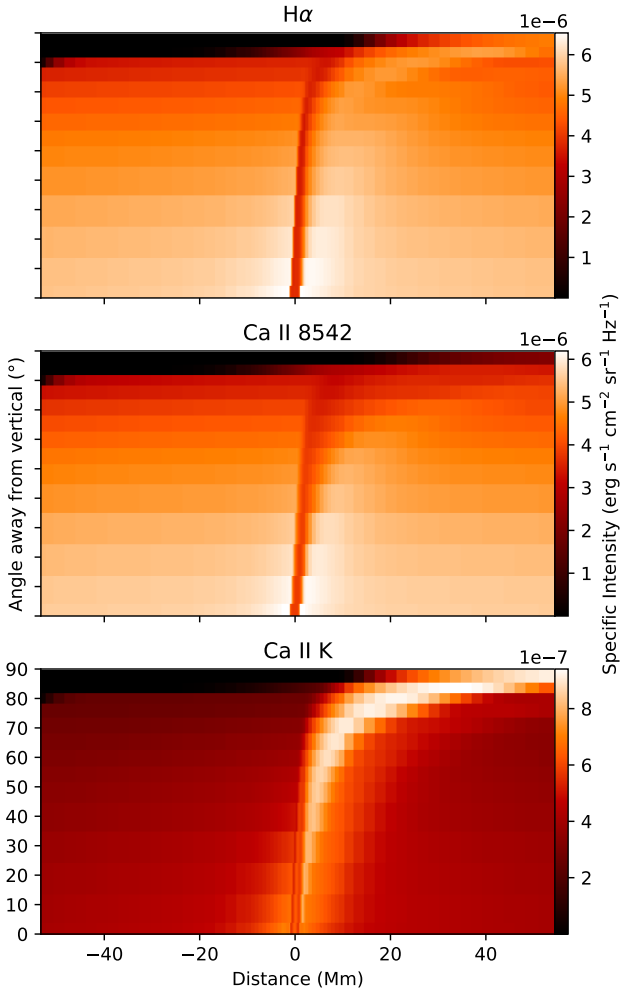

Figure 2. Spatial and angular variation of the Hα, Ca II 8542 & K spectral line intensities I_e emerging from the 'toy' prominence model of Figure 1. For each spectral line, from the bottom to top-most row the LOS rotates from vertical to horizontal. Symmetric brightenings are present either side of the filament absorption for $\mu_z = 1 \rightarrow \theta_z = 0°$, becoming increasingly antisymmetric and comprised of fine structures, that vary depending on the spectral line, as the viewing angle increases.

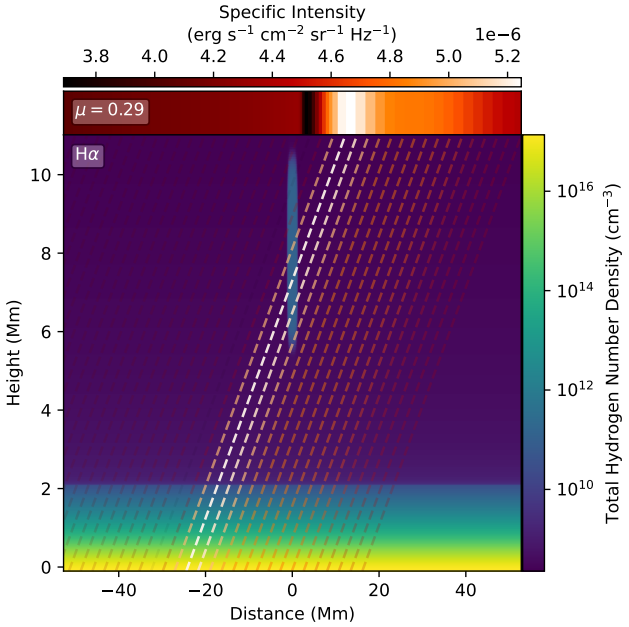

Figure 3. Source of intensity enhancements present next to central filament absorption. *Top panel*; Emergent intensity I_e of the Hα transition at a slightly inclined viewing angle of $\mu = 0.29$ to the vertical. *Bottom panel*; Model total hydrogen number density, with dashed lines overlaid to indicate the intersection between the LOS and features within the domain. The lines are additionally coloured according to the intensity within the upper panel, and their transparency set to emphasise the brighter LOS. The broader Hα intensity enhancement comes from the chromosphere beneath the prominence, whereas the brighter enhancement comes directly from the prominence underside.

3.2. *Spatial and Angular I_e variations*

The top panel of Figure 2 presents the line core emergent intensity I_e of the Hα transition at a range of observing angles into the top of the 'toy' prominence model domain of Figure 1 (cf. Fig. 4 of Libbrecht et al. 2021). The bottom row of this panel describes the intensity emerging exactly vertically ($\mu_z = 1 \rightarrow \theta_z = 0°$). The absorption profile for the filament at 0 Mm is apparent but made more obvious by the larger intensities (in comparison with the edge of the synthesis domain at 55 Mm) that border it. The y-axis of the same plot then describes how this emergent intensity changes for an increasing viewing angle of the observer (decrease μ_z) towards the horizontal. The intensity increase flanking the absorption profile becomes increasingly asymmetric as the LOS is inclined through $0-40^\circ$, migrating in the + Distance direction. After 40°, this enhancement becomes simultaneously weaker and more diffuse as a combined consequence of the inclined viewing angle (limb-darkening) and the coarser spatial resolution through which the radiative transfer is calculated, respectively. At approximately 60° a second bright feature is identifiable now closer to the filament absorption, and becomes increasingly visible against the first as the viewing angle increases past this point. As the inclination approaches 80°, the portions of the LOS that are at X < -50 Mm begin to miss the solar disk altogether and thus have zero intensity. As the inclination approaches 90°, the prominence transitions from the filament to prominence projection, instead appearing bright against the background of space. The remainder of the Figure presents the equivalent appearance and angular-variation for the Ca II 8542 Å & K line cores. The broader intensity en-

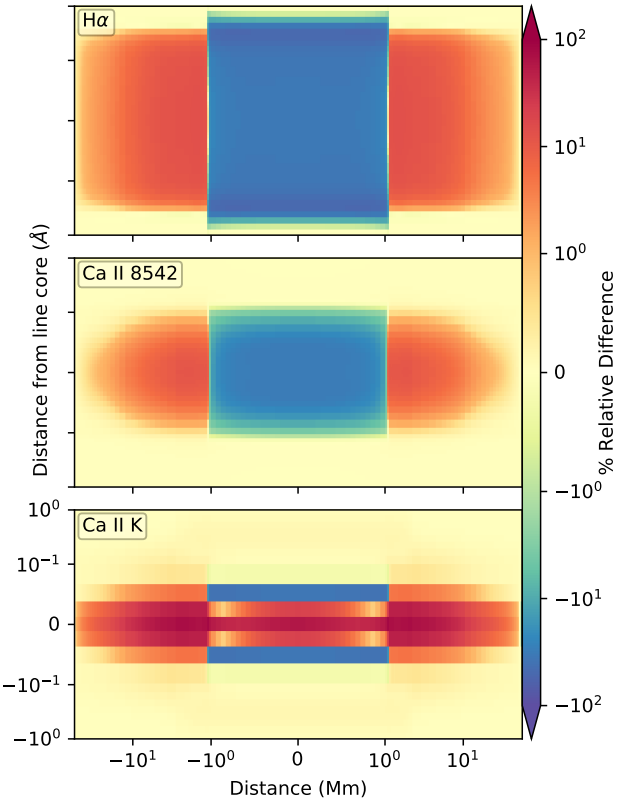

Figure 4. Spatial and spectral variation of the Hα, Ca II 8542 & K spectral line % relative differences in I_e for $\mu_z = 1$ compared to a chromosphere-only domain, positive indicating brighter and vice versa.

hancement remarked to flank the central absorption of the filament is present in each case. The thinner enhancement that appeared past 60° is entirely absent for the Ca II 8542 Å intensity. For Ca II K, on the other hand, this feature is present almost from the moment the LOS deviates from the exact vertical and strongly dominates the emergent intensity thereafter, essentially rendering the prominence as an emission feature against the background solar chromosphere. We will discuss this in more detail in Section 4.

In the upper strip of Figure 3 we zoom in on the single viewing angle of $\mu = 0.29$ for the Hα emergent intensity. Here, the intensity limits are now tuned to the maximum and minimum of this singular strip rather than all strips, better highlighting the variations herein. At this viewing angle, the two aforementioned bright components are clearly identified as a superposition of a broad enhancement that spans from the filament absorption to approximately 40 Mm, and a thinner brighter enhancement that spans approximately 5 – 15 Mm. In the bottom panel of total hydrogen number density, from the traced rays, we see that the broader enhancement is sourced from the chromosphere underneath the prominence whereas the brighter enhancement is instead from the lower portions of the prominence body itself. Furthermore, at this angle, the filament absorption appears to correspond to only the upper portions of the prominence body.

3.3. *Spectral I_e variations*

In Figure 2 we found a spatially symmetric enhancement flanking the central filament absorption feature at a viewing angle of 0°. In Figure 4, we expand to include the wavelength dimension and present the % relative difference in I_e against a pre-relaxed chromosphere-only domain, where the spatial and spectral scaling is now log – log to emphasise the spatial and spectral cores of the prominence and spectral lines, respectively. The model of Figure 1 contains zero velocities throughout the domain, so the spectral profiles of all the transitions shown are expectedly symmetric about their rest wavelength for all spatial positions. The intensity variations in both space and wavelength are symmetric about 0 for $\mu = 1$, yet the enhancement is wavelength dependent with the largest spatial extent being in each case at the line core wavelength. For Hα, we see that as the spatial distance from the prominence body increases, the relative difference drops to 0 closer to the line core, an identical feature yet more pronounced for both the Ca II 8542 & K lines. For the Ca II K transition, a more complex situation appears present, with the gradated central line core enhancements giving way to relative decreases at larger $\Delta\lambda$. The wavelength sampling employed in the spectral integration of the radiative rates is quite insufficient for further analysis of the Ca II K transition, though this will be discussed in more detail in Section 4.

4. SUMMARY AND DISCUSSIONS

It was previously shown by Jenkins et al. (2023) that a 1.5D approach to a combined chromosphere + prominence atmosphere suffers from artificial radiation trapping/pumping caused by the infinite plane-parallel assumption (with relevance to *e.g.*, Díaz Baso et al. 2019). This indicated that a radiative connection existed between the solar chromosphere + prominence, as previously hinted at by Paletou (1995). To further explore this a 2.5D domain was required so that both the partial radiation trapping and the finite extent of the prominence could be represented within the same model. The aim of this manuscript was to adopt the 2.5D *Lightweaver* radiative transfer framework, apply it to a specific case-study 'toy' prominence model, quantify the degree of chromosphere – prominence connection

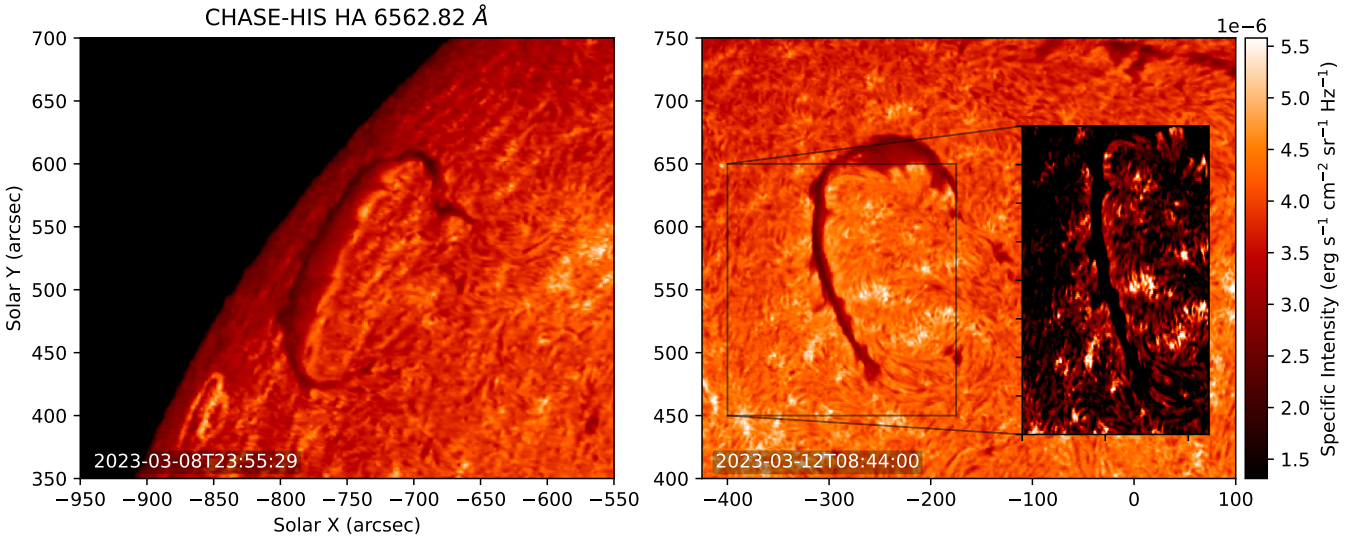

Figure 5. Two CHASE/HIS observations of the same prominence exhibiting the bright-rim phenomenon on 2023-03-08 and 2023-03-12. At the earlier time, the filament was located at $\approx 60^{\circ}$. For the later time, the filament was located at $\approx 20^{\circ}$. The intensity of the filament observation in the inset of the right panel has been saturated to emphasise the brightenings on either side of the filament body.

present, and demonstrate the utility of this approach in further exploring the as-yet insufficiently explained 'bright-rim' prominence phenomenon.

In relaxing the atomic transitions to statistical equilibrium in 2.5D, aided by the initial conditions available within the Heinzel et al. (2015) 1D NLTE radiative transfer solutions, we began by confirming the electron number density n_e to be significantly modified within the prominence (as previously stated by Paletou 1995, and subsequently shown by Léger et al. 2007, to be a consequence of photoionisation). Unlike the 1D models of Heinzel et al. (2014) or Zapiór et al. (2016), however, the degree of enhancement that both Léger et al. (2007) and we find within the prominence and/or PCTR appears less pronounced. That said, the models of Gouttebroze et al. (1993) already demonstrated that such enhancements can vary significantly even in 1D, and our 'toy' model represents but a single idealised case study; the parameter space of photoionisation behaviour in multidimensional prominence models requires further exploration. As our 2.5D domain integrates both the chromosphere and the prominence, we confirm and expand upon the predicted prominence backscattering of Paletou et al. (1993), demonstrated here using the albedo of the Lyman continuum head in Figure 1, in its capacity of pumping the population of n_e within the chromosphere. This excess is most pronounced underneath the prominence and decreases with increasing distance.

In Figure 2 we found that the locations of increased n_e within the chromosphere overlap with the regions of increased emergent intensity I_e that flank the central filament absorption for a viewing angle of $\mu_z = 1$. By increasing the viewing angle towards the horizontal, we saw that such brightenings become increasingly asymmetric and skewed in the direction of the observer. At $\mu_z = 0.29$, and as shown in Figure 3, a second more intense brightening becomes clearly visible closer to the filament absorption signature. In the same figure, we showed that the more diffuse brightening originates from the underlying chromosphere (as previously argued by Kostik & Orlova 1975 and Panasenco 2010) whilst the brighter and more-localised intensity enhancement is sourced in the underside of the prominence itself (closer to the interpretation of Heinzel et al. 1995, albeit contested by Paletou 1997).

In Figure 4, we explored the difference in appearance of the diffuse brightenings that flank the filament absorption for a viewing angle of $\mu_z = 1$. For each of the spectral lines shown, we found their % relative difference to range between a few % to more than 100%. These brightenings then have the largest extent for the line core wavelength, likely as a consequence of the prominence being the most optically-thick and/or scattering in the line core. As such, the exact magnitude and extent of these brightenings must depend on numerous aspects of the prominence atmosphere, and will require a theoretical effort as by Gouttebroze et al. (1993) to understand them better.

The next step in the process of proving the theoretical aspects highlighted in this manuscript is to compare directly with observations. We envision a statisti-

cal study, that will take into account a range of observed prominences that exhibit the bright-rim phenomenon. A host of historical observations are available through the GONG Hα network (Harvey et al. 2011). Of particular interest is the *Hα Imaging Spectrograph* (HIS; Liu et al. 2022) instrument onboard the *Chinese Hα Solar Explorer* (CHASE; Li et al. 2022) satellite, a slit spectrograph that captures the most spectrally pure observations of the Hα line to date. Launched in 2021, it has already collected an extensive database of observations, both synoptic and dedicated, that is now publicly available[2]. In Figure 5 we present two observations of a solar prominence taken with the HIS instrument. The entire disk passage of this prominence was recorded by the instrument, but we focus here on two specific times. The first, presented in the left panel, is from 08 March 2023 when the prominence was close to the limb ($\approx 60^{\circ}$) but still projected against the solar disk as a filament. At this time, the prominence is exhibiting the characteristic 'bright-rim' phenomenon where the lowermost portion of the structure appears bright against both the prominence itself and the underlying solar chromosphere. The second, presented in the right panel, is from 12 March 2023 when the same prominence is near disk-center ($\approx 20^{\circ}$). At this time, there is no appearance of a 'bright-rim' as typically described. Inline with the discussion of Panasenco et al. (2014), however, by saturating the intensities of this observation we can reveal coherent brightenings that trace the outline of the prominence body, reminiscent of the more symmetric brightenings of Figure 2.

Finally, it is clear that the appearance of the Ca II K line in Figure 4, and especially Figure 2, somewhat contradicts what we have come to anticipate from observations of solar prominences. That is, the on-disk projection of a prominence (filament) in Ca II K is almost exclusively an absorption signature yet appears in both figures with a positive constrast against the chromosphere (cf. Kuckein et al. 2016; Chatterjee et al. 2017; Chatzistergos et al. 2023). For an identical model with an internal prominence pressure of 0.1 dyn cm^{-2}, not explicitly shown here, we recover once more an absorption signature for the Ca II K line. It is clear that the 'toy' model that we have adopted here, albeit employed as a proof of concept, is lacking a crucial dimension of realism. One possibility is the idealised thermodynamic properties of the prominence, in particular the lack of an MHS initial condition (such as in Heinzel & Anzer 2001) or a self-consistent MHD solution (cf. Jenkins & Keppens 2021, 2022). Another, as the latter works also highlight, is the assumed prominence topology of a monolithic versus threaded body, altering the opacity distribution along the LOS and hence the radiative behaviour (in line with the recent work of Peat et al. 2023). Furthermore, although the numerical resolution of the model was deliberately focused at the PCTR, these authors have also shown that such a region can have a dimension of a few tens of km, far below the resolution of our model. Each of these aspects will receive dedicated attention moving forward.

[2] Solar Science Data Center of Nanjing University

ACKNOWLEDGEMENTS

RK and JMJ are supported by the ERC Advanced Grant PROMINENT and an FWO grant G0B4521N. This project has received funding from the European Research Council (ERC) under the European Union's Horizon 2020 research and innovation programme (grant agreement No. 833251 PROMINENT ERC-ADG 2018). This research is further supported by Internal funds KU Leuven, project C14/19/089 TRACESpace. The computational resources and services used in this work were provided by the VSC (Flemish Supercomputer Center), funded by the Research Foundation Flanders (FWO) and the Flemish Government – department EWI. CMJO acknowledges support from the University of Glasgow's College of Science and Engineering. CHASE mission is supported by China National Space Administration (CNSA). CL and YQ are supported by NSFC under grant 12333009 and CNSA project D050101.

Facilities: Vlaams Supercomputer Centrum, CHASE/HIS

Software: Python (Van Rossum & Drake Jr 1995), Lightweaver (Osborne & Milić 2021), Numpy (Harris et al. 2020), Matplotlib (Hunter 2007), yt-project (Turk et al. 2011)

REFERENCES

Bruls, J. H. M. J., Vollmöller, P., & Schüssler, M. 1999, A&A, 348, 233

Carlson, B. C. 1963, Methods for Computational Physics (New York: Academic Press)

Carlsson, M., & Leenaarts, J. 2012, A&A, 539, A39, doi: 10.1051/0004-6361/201118366

Carlsson, M., Fletcher, L., Allred, J., et al. 2023, A&A, 673, A150, doi: 10.1051/0004-6361/202346087

Chatterjee, S., Hegde, M., Banerjee, D., & Ravindra, B. 2017, ApJ, 849, 44, doi: 10.3847/1538-4357/aa8ad9

Chatzistergos, T., Ermolli, I., Banerjee, D., et al. 2023, A&A, 680, A15, doi: 10.1051/0004-6361/202347536

De Ceuster, F., Homan, W., Yates, J., et al. 2020, MNRAS, 492, 1812, doi: 10.1093/mnras/stz3557

Díaz Baso, C. J., Martínez González, M. J., Asensio Ramos, A., & de la Cruz Rodríguez, J. 2019, A&A, 623, A178, doi: 10.1051/0004-6361/201834793

Górski, K. M., Hivon, E., Banday, A. J., et al. 2005, ApJ, 622, 759, doi: 10.1086/427976

Gouttebroze, P. 2006, A&A, 448, 367, doi: 10.1051/0004-6361:20054139

Gouttebroze, P., Heinzel, P., & Vial, J. C. 1993, A&AS, 99, 513

Harris, C. R., Millman, K. J., van der Walt, S. J., et al. 2020, Nature, 585, 357, doi: 10.1038/s41586-020-2649-2

Harvey, J. W., Bolding, J., Clark, R., et al. 2011, in AAS/Solar Physics Division Abstracts #42, AAS/Solar Physics Division Meeting, 17.45

Heinzel, P., & Anzer, U. 2001, A&A, 375, 1082, doi: 10.1051/0004-6361:20010926

Heinzel, P., Gunár, S., & Anzer, U. 2015, A&A, 579, A16, doi: 10.1051/0004-6361/201525716

Heinzel, P., Kotrč, P., Mouradian, Z., & Buyukliev, G. T. 1995, SoPh, 160, 19, doi: 10.1007/BF00679090

Heinzel, P., Zapiór, M., Oliver, R., & Ballester, J. L. 2014, A&A, 562, A103, doi: 10.1051/0004-6361/201322346

Hunter, J. D. 2007, Computing in Science & Engineering, 9, 90, doi: 10.1109/MCSE.2007.55

Jaume Bestard, J., Štěpán, J., & Trujillo Bueno, J. 2021, A&A, 645, A101, doi: 10.1051/0004-6361/202039424

Jenkins, J. M., & Keppens, R. 2021, A&A, 646, A134, doi: 10.1051/0004-6361/202039630

—. 2022, Nature Astronomy, 6, 942, doi: 10.1038/s41550-022-01705-z

Jenkins, J. M., Osborne, C. M. J., & Keppens, R. 2023, A&A, 670, A179, doi: 10.1051/0004-6361/202244868

Keppens, R., Popescu Braileanu, B., Zhou, Y., et al. 2023, A&A, 673, A66, doi: 10.1051/0004-6361/202245359

Kippenhahn, R., & Schlüter, A. 1957, ZA, 43, 36

Kostik, R. I., & Orlova, T. V. 1975, SoPh, 45, 119, doi: 10.1007/BF00152223

Kuckein, C., Verma, M., & Denker, C. 2016, A&A, 589, A84, doi: 10.1051/0004-6361/201526636

Léger, L., Paletou, F., & Navarre, F. 2007, in SF2A-2007: Proceedings of the Annual meeting of the French Society of Astronomy and Astrophysics, ed. J. Bouvier, A. Chalabaev, & C. Charbonnel, 592

Li, C., Fang, C., Li, Z., et al. 2022, Science China Physics, Mechanics, and Astronomy, 65, 289602, doi: 10.1007/s11433-022-1893-3

Libbrecht, T., Bjørgen, J. P., Leenaarts, J., et al. 2021, A&A, 652, A146, doi: 10.1051/0004-6361/202039788

Liu, Q., Tao, H., Chen, C., et al. 2022, Science China Physics, Mechanics, and Astronomy, 65, 289605, doi: 10.1007/s11433-022-1917-1

Osborne, C. M. J., & Fletcher, L. 2022, MNRAS, 516, 6066, doi: 10.1093/mnras/stac2570

Osborne, C. M. J., & Milić, I. 2021, ApJ, 917, 14, doi: 10.3847/1538-4357/ac02be

Paletou, F. 1995, A&A, 302, 587

—. 1997, A&A, 317, 244

Paletou, F., Vial, J. C., & Auer, L. H. 1993, A&A, 274, 571

Panasenco, O. 2010, Mem. Soc. Astron. Italiana, 81, 673

Panasenco, O., Martin, S. F., & Velli, M. 2014, SoPh, 289, 603, doi: 10.1007/s11207-013-0337-1

Parenti, S. 2014, Living Reviews in Solar Physics, 11, 1, doi: 10.12942/lrsp-2014-1

Peat, A. W., Labrosse, N., & Gouttebroze, P. 2023, arXiv e-prints, arXiv:2310.08249, doi: 10.48550/arXiv.2310.08249

Turk, M. J., Smith, B. D., Oishi, J. S., et al. 2011, ApJS, 192, 9, doi: 10.1088/0067-0049/192/1/9

Van Rossum, G., & Drake Jr, F. L. 1995, Python reference manual (Centrum voor Wiskunde en Informatica Amsterdam)

Vernazza, J. E., Avrett, E. H., & Loeser, R. 1981, ApJS, 45, 635, doi: 10.1086/190731

Vial, J.-C., & Engvold, O. 2015, Solar Prominences (Springer)

Štěpán, J., Jaume Bestard, J., & Trujillo Bueno, J. 2020, A&A, 636, A24, doi: 10.1051/0004-6361/202037566

Štěpán, J., & Trujillo Bueno, J. 2013, A&A, 557, A143, doi: 10.1051/0004-6361/201321742

Xia, C., Chen, P. F., & Keppens, R. 2012, ApJ, 748, L26, doi: 10.1088/2041-8205/748/2/L26

Zapiór, M., Oliver, R., Ballester, J. L., & Heinzel, P. 2016, ApJ, 827, 131, doi: 10.3847/0004-637X/827/2/131